



# Custom density fluorescent tracer fabrication via microfluidics

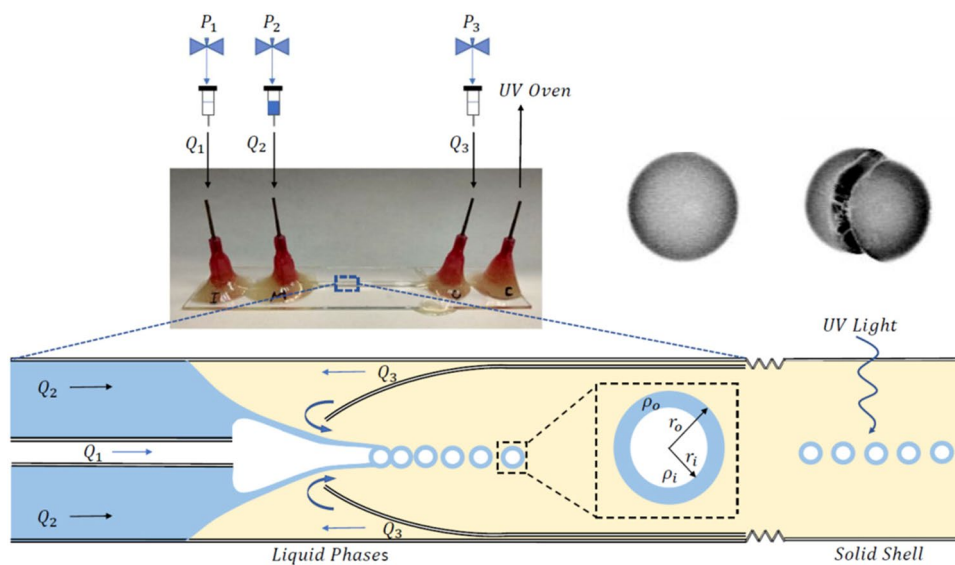
Meiran Miezner<sup>1</sup> · Subhani Shaik<sup>1</sup> · Ian Jacobi<sup>1</sup>

Received: 25 September 2020 / Revised: 17 January 2021 / Accepted: 15 February 2021 / Published online: 7 April 2021  
© The Author(s), under exclusive licence to Springer-Verlag GmbH, DE part of Springer Nature 2021

## Abstract

A microfluidic system for creating custom density tracer particles with low polydispersity is described in which the particle density can be fine-tuned by varying the salt concentration in the core of a double-emulsion droplet. The droplets are generated in a glass-capillary, co-flow device and then solidified lithographically for use in a variety of flow experiments, including particle-image velocimetry and multi-phase flows. The novel use of solidified, double-emulsion droplets for flow tracers provides precise control of particle density, size, shape and fluorescent properties in a form that can be easily implemented in standard, macroscale laboratory settings.

## Graphic abstract



**Keywords** Multi-phase flow · Particle image velocimetry · Microfluidics · Droplets

## 1 Introduction

Microscopic, solid particles are essential features of macroscale, experimental fluid systems, both as diagnostic tracers for single-phase flow analysis and as a constituent phase in

multi-phase flows. For single-phase flows, solid particle tracers are used for full-field velocity measurement techniques including particle-image (Adrian and Westerweel 2010) and particle-tracking (Dabiri and Pecora 2019) velocimetry, where the particles are assumed to behave as passive elements, faithfully following the underlying fluid motion. The fidelity of the representation of the flow depends on both the mechanical properties of the particle and the dynamics of the flow field itself (Mei 1996) and has historically been

✉ Ian Jacobi  
ijacobi@technion.ac.il

<sup>1</sup> Faculty of Aerospace Engineering, Technion Israel Institute of Technology, Haifa 32000, Israel

described by a characteristic frequency of the fluid,  $\omega$ , its kinematic viscosity,  $\nu$ , and the radius of the particle,  $r$ , which together can be used to define a Stokes number,  $St = \sqrt{4\omega r^2/\nu}$ . In turbulent flows, the Stokes number, in conjunction with an approximation of the spectral energy density of the flow,  $E(\omega)$ , and the ratio,  $s = \rho_p/\rho_f$ , of the particle density,  $\rho_p$ , to fluid density,  $\rho_f$ , can be used to approximate the ratio of particle velocity fluctuations to fluid fluctuations,  $\overline{u_p^2}/\overline{u_f^2}$  and thus the fidelity of the tracer (Melling 1997). As  $s$  approaches unity, the particles are predicted to follow the fluid motion exactly.

The strong dependence of the tracer fidelity on the density ratio,  $s$ , has motivated a variety of different commercially available tracer options in liquid flows, ranging from aluminum or titanium dioxide particles to hollow glass or polystyrene microspheres. The latter microsphere options are widely used in water flows since they are close to neutrally buoyant ( $s \approx 1$ ), thereby producing a high frequency response to fluctuations in the surrounding fluid.

In multi-phase flows, non-neutrally buoyant particles are often desirable for studying the interaction between inertial particles and the coherent structures in the surrounding flow (Eaton and Fessler 1994; Crowe et al. 1985; Hetsroni 1989), which can have important consequences for the modulation of the turbulence (Zhao et al. 2010; Lee and Lee 2015) and the transport and deposition of particles on substrates (Guha 2008). The challenge in full-field measurement of particle-laden flows is to measure the velocity field using a passive tracer, as in the single-phase problem, and simultaneously to measure the dynamics of the inertial particles constituting the dispersed phase.

Many approaches have been used for distinguishing between tracer particles and inertial particles, including most prominently fluorescent tracers and digital phase separation via masking (Lindken and Merzkirch 2002; Cheng et al. 2010). When fluorescent tracers are illuminated at incident wavelength  $\lambda_i$ , they emit light at wavelength,  $\lambda_e$ , different from the light reflected at  $\lambda_i$  by the (non-fluorescent) inertial particles in the flow. Thus, the two types of particles can be separated by optical filtering with two cameras focused on the same spatial domain. Digital masking is performed by the use of an additional step in the PIV algorithm that discriminates between different particles by size or light intensity (Khalitov and Longmire 2002). A combination of these two techniques has also been used (Elhimer et al. 2017; Hoque et al. 2016).

In order to employ these techniques, particles must be obtained that vary in size, reflective or fluorescent properties, and density constraints, which are not easily satisfied by commercially available particles. Dying commercial glass particles with fluorescent dye (Kondo and Miyamoto 2017), grinding and sieving fluorescently dyed plastics (Pedocchi et al. 2008), or melting and dispersing wax droplets (Tauro et al. 2013)

provide simple techniques for generating custom particles, but offer limited control of density and polydispersity.

In contrast, microfluidic techniques provide complete control over all of the properties of custom particles. While microfluidic tools have long been used for the generation of liquid microdroplet emulsions, lithography can be used to cross-link polymer droplets into solid particles (Nisisako et al. 2004) of any shape (Dendukuri et al. 2006). And, unlike single-emulsion droplets, double-emulsion droplets provide an additional degree of design freedom during the droplet generation, allowing for modifying optical and mechanical properties of the droplet, due to the different properties of the inner and outer droplet phases. The different phases of double-emulsion droplets have also been used to improve the output of single-phase droplets, after the outer phase is evaporated (Nan et al. 2020). Moreover, double-emulsion droplets can be generated easily without any special microfluidic equipment, using simple glass capillaries (Utada et al. 2005) and laboratory air pressure (Bong et al. 2011).

We apply an inexpensive, microfluidic, double-emulsion droplet generation technique with lithography to generate custom size and density, solid microparticles with tunable fluorescence, for use in large-scale multi-phase flow experiments. Although double-emulsion droplets have been used widely in microscale fluids and chemistry research, the approach described here involving precision density control of the inner phase marks a new application of double-emulsion droplets to significantly improve on the state of the art in macroscale tracer particles. In Sect. 2, we describe the construction of a simple microfluidic device capable of generating tunable particles; in Sect. 3, the mechanical and fluorescent properties of the particles are characterized, and pump and pressure generation systems are compared. In Sect. 4, two sets of particles generated with distinct densities are optically distinguished by their fluorescent properties in a simple, settling demonstration.

## 2 Particle generation

Double-emulsion droplets contain both inner (subscript  $i$ ) and outer (subscript  $o$ ) dispersed phases, appearing as a sphere with a concentric, spherical shell, immersed in a continuous phase. The key approach employed here for obtaining independent control of the overall density of the particle and its fluorescent properties is to select an outer phase for the shell that can be fluorescently dyed and lithographically solidified, with an inner phase whose density can be easily and precisely modified over a wide range of specific gravities. The outer phase is a photo-sensitive polymer solution combined with oil-soluble, fluorescent dye, and the inner phase is a water-based salt solution.

By varying the concentration of the salt, the density of the inner solution,  $\rho_i$ , can be precisely tuned. The outer solution density,  $\rho_o$ , is roughly constant (depending on the dye concentration). The average density of the resulting double-emulsion droplet,  $\bar{\rho}$ , is then calculated from the densities of the two solutions and the radii of the nested droplets,  $r_i$  and  $r_o$ , according to:

$$\bar{\rho} = \rho_o + \left(\frac{r_i}{r_o}\right)^3 (\rho_i - \rho_o) = \rho_o + \Delta\rho \left(1 + \frac{\Delta r}{r_i}\right)^{-3}. \quad (1)$$

The average density of the particle therefore depends on the thickness of the outer fluid shell,  $\Delta r = r_o - r_i$ , relative to the inner radius, in addition to the density contrast between the two solutions,  $\Delta\rho = \rho_i - \rho_o$ . However, because  $\Delta r/r_i \ll 1$  in most cases, the overall density primarily depends on the density contrast and is thus largely controlled by the salt concentration in the inner phase.

The inner salt solution was formulated based on the commercially available salt with the highest density and highest solubility in water, cesium chloride (Carl Roth # 7878.1, density: 3.983 kg/L; solubility 1.91 kg/L at 25° C). The salt solution must be combined with surfactant (polyvinyl alcohol (PVA) Mowiol 8-88, Sigma-Aldrich # 81383) in order to generate stable droplets. As the quantity of salt increases, the solubility of the surfactant decreases, and for the minimum necessary surfactant concentration of 0.3% w/w found for this system, the maximum salt concentration achievable was 27% w/w before the surfactant would precipitate out of solution. Increasing the surfactant concentration generally improves the long-term stability of thin-shelled droplets (Zhao et al. 2017), although in this system the droplets need to remain stable for only seconds before the shell is solidified.

The purpose of the outer phase is to exhibit desired fluorescent or reflective properties while hardening into a solid shell via exposure to light. Therefore, the outer phase was formulated from a liquid polymer (TRPGDA—tri(propylene glycol) diacrylate, Sigma-Aldrich #246832) and UV-sensitive cross-linking agent (HMPP—2-hydroxy-2-methylpropiophenone, Sigma-Aldrich #405655), to which was added

an oil-soluble fluorescent dye (Nile Red, Sigma-Aldrich # 72485). The cross-linker rapidly solidifies the liquid polymer, upon exposure to UV light, into a solid plastic, without bleaching the fluorescent dye. To create the fluorescent polymer solution, the solid dye was first dissolved in a cosolvent (acetone, Gadot #200-662-2, 67-64-1) until its solubility limit (1.5 mg/mL). The fluorescent acetone was then mixed very gradually into the liquid polymer, at a rate of 5 mL/day, to allow the acetone to evaporate, leaving the dye in solution primarily with the polymer at a concentration of 0.3% w/v. After the polymer was dyed, the cross-linking agent was added at a ratio of 4% v/v, and the solution was filtered twice, using 0.45  $\mu\text{m}$  and then 0.22  $\mu\text{m}$  filters. Dimethyl sulfoxide (DMSO) (Sigma-Aldrich #276855) was also tested as a cosolvent, although its lower volatility means more remained in the final outer phase, compared to the acetone. Also, other oil-soluble fluorescent dyes (e.g., commercially available Dye-Lite by Tracer Products for visible wavelength excitation; coumarin VI, Sigma-Aldrich #442631, for UV excitation) were also shown to be compatible with the production system (details not reported here).

The continuous phase for the double-emulsion droplets was DI water with the same surfactant used in the salt solution. Measurements of fluid densities (using a Ludwig Schneider Hydrometer) and interfacial tensions (with a Biolin Scientific Theta Lite Tensiometer) for each of the phases, along with their detailed compositions, are listed in Table 1.

The double-emulsion droplets were produced using a simple, co-flow microfluidic device constructed from commercially available glass capillaries (Utada et al. 2005), although any of the wide variety of droplet production techniques could also be employed (Chong et al. 2015). A round glass capillary tube (CM Scientific Ltd.-Round Boro Tubing, 0.7 ID, 0.87 OD) was pulled with a capillary puller (Sutter P-97) to generate two identical tubes, each with a narrow tip on one end. The tips were then cut using a glass-on-glass scoring technique to obtain a 50 – 100  $\mu\text{m}$  diameter outlet for the inner phase and a 200 – 300  $\mu\text{m}$  diameter receiver for the complete droplets. The outlet tip was given a hydrophobic surface treatment (Aqua-Pel), after which the two round capillaries were aligned inside a square capillary

**Table 1** The composition and properties for the three phases of the droplet production, including three possible variations of the inner phase, using deionized water (DI, density: 0.997 g/mL) with and without salt at its solubility limit. Interfacial tension was measured with respect to the outer phase solution

Solution	Composition	Density [g/mL]±0.002	Viscosity [mPa·s]	Interfacial tension [mN/m]
Inner	DI+0.3% w/w PVA	0.996	1.62 ± 0.09	23.7 ± 0.5
Inner	DI+2% w/w PVA	1.000	3.4 ± 0.1	26 ± 1
Inner	DI+27% w/w CsCl+0.3% w/w PVA	1.258	2.1 ± 0.4	3.5 ± 0.2
Outer	TRPGDA+0.3% w/v Nile Red +4% v/v HMPP	1.032	15 ± 1	–
Continuous	DI+10% w/w PVA	1.012	86 ± 3	48.9 ± 0.6

tube (CM Scientific Ltd.- Square Boro, ID:  $0.90 \times 0.90$  mm, wall thickness 0.18 mm) and the three tubes were glued to a microscope slide for structural support. Blunt-end syringe tips (Instech LS20 Luer stubs) were glued to the slide over the inlet and outlet ends of the capillaries to seal the system and allow the solutions to be pumped into the capillaries by attaching tubing to the syringe tips (Instech—BTPE-90 polyethylene tubing). The capillary device and its corresponding flow field are illustrated in Fig. 1. The entire construction can be performed, in principle, in an ordinary, non-microfluidic laboratory. As the three phases are pumped through the capillary, double-emulsion droplets form via flow focusing. The average droplet dimensions can be regulated by changing the flowrates of the fluids and the size of the glass capillary nozzle (Utada et al. 2007).

The capillary device was supplied with the three solutions by one of two different pumping systems: a volumetric system, consisting of three syringe pumps (Fusion 720 and Nexus 6000, Chemyx Inc), and a pressure-driven system, using the laboratory air pressure and a series of regulators (ControlAir 120-BA) and gauges (Dwyer DPGA-05 0-15 psig). The pressure-driven flow system was based on previously reported designs for highly accurate supply of low flowrates (Bong et al. 2011), but was modified with additional, independent pressure regulators to allow for maintaining vastly different flowrates between the different solutions. Guidelines for the flowrates and pressures needed to obtain droplets with outer diameters in the range of 60–100  $\mu\text{m}$  are

provided in Table 2 in appendix. After the double-emulsion droplets exit the capillary device, they pass through a UV curing oven (Uvitron International—Intelli-Ray 400) where they are exposed for about 15–20 s to cure the outer shells before being collected.

The droplet production rate can be estimated from the flowrates of the two droplet phases and the average size of the droplets, or from direct microscopic observation (described below). The production rate was typically between 1300 and 1600 droplets/s, which would produce 1 g of neutrally buoyant, 70- $\mu\text{m}$ -diameter particles in about 40–50 minutes on a single device.

In order to calculate the average density of the produced particles, following equation 1, the inner and outer radii of the droplets must be accurately measured. This can be performed with a simple benchtop microscope, but for the purpose of resolving the fluorescent and non-fluorescent solutions separately, scanning the fluorescence response (described below), and making time-resolved measurements, we used a confocal scanning microscope (TCS SP8, Leica Microsystems) with two different objective lenses (Leica HC PL Fluator 10X/0.3 and HC PL Fluator 5X/0.15). The cross section of the droplets was recorded using the minimum confocal pinhole, thereby minimizing the section thickness of the scan to a fraction of the droplet outer diameter, from which the radii of the droplets were extracted.

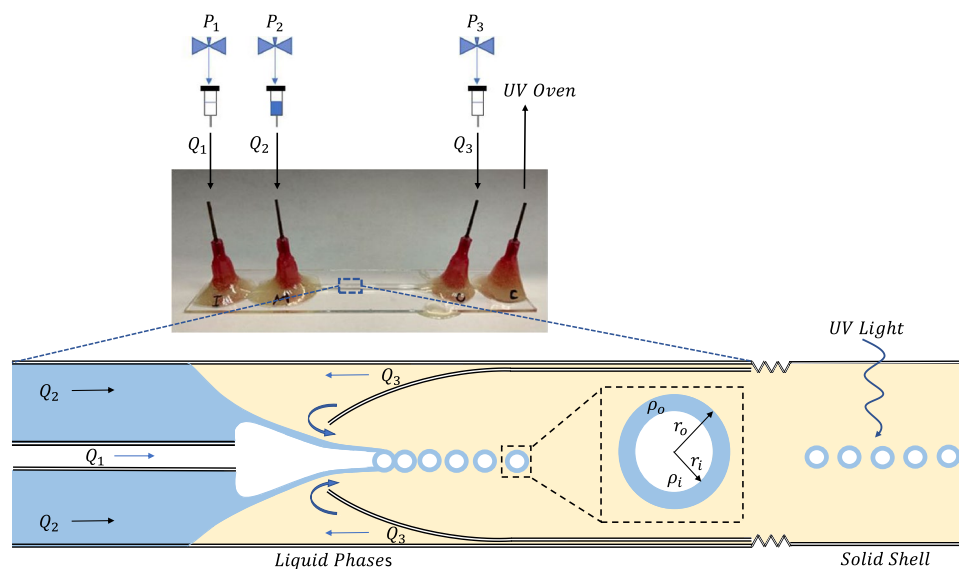


**Fig. 1** The double-emulsion droplet production system consists of a glass capillary device, shown in the picture, attached to three pressure regulators connected to syringes filled with the three solutions. The double-emulsion droplets formed in the device proceed to a UV oven for curing, hardening the outer shell, after which they are collected in a vial.  $Q_1$  is the inner salt-water solution;  $Q_2$  is the outer polymer

solution;  $Q_3$  is the continuous-phase water solution. The two inner jets focused by the outer flow break into concentric droplets, as illustrated in the left side of the lower cartoon, representing the nozzle region of the capillary device; on the right, representing a far-downstream region, the UV irradiation is sketched, where the droplets become solid

### 3 In situ particle characterization

Measuring the radii of the particles during the production process, within the capillary device, allows for simultaneous measurement of the rate of droplet production, time-resolved polydispersity, and the spatially evolving geometry of the droplets. However, this *in situ* measurement of moving droplets poses unique measurement challenges.

The confocal microscope does not capture the entire interrogation window instantaneously, but rather scans the area in sequential lines at a fixed frequency, e.g.,  $f_{scan} = 1.2 \times 10^4$  px/s, in one direction, doubled for bidirectional scanning. The velocity at which the scan line proceeds across the interrogation window depends on the objective, which determines the scan resolution, e.g.,  $r = 1.13 \mu\text{m}/\text{px}$ , and is given by  $v_{scan} = r f_{scan}$ . As the droplet moves across the interrogation window, opposite to the scan direction and orthogonal to the scan lines, its image becomes artificially shortened, as illustrated in cartoon form in Fig. 2. Motion parallel to the scan lines causes even more complicated shear distortions and should be avoided. Optical distortion due to the different indices of refraction of the capillary system was negligible compared to the scanner distortion.

The confocal scan distortion factor,  $\alpha$ , relates the true length in the scan/flow direction,  $d$ , to the perceived length in the microscope image,  $d_{image}$ , as  $d = \alpha d_{image}$ , where  $\alpha$  can be expressed in terms of the velocity of the droplet,  $v_{droplet}$ , and the scan velocity,  $v_{scan}$ , by:

$$\alpha = 1 + \frac{v_{droplet}}{v_{scan}} \tag{2}$$

The magnitude of the scan distortion decreases as the droplets slow down, downstream of the collection tip, where the capillary inlet widens to its full diameter. Indeed, the  $\alpha$  factor can be predicted from mass conservation and the measured inner radius of the capillary, as show in the red line in Fig. 3. The predicted  $\alpha$  is plotted against a calculated  $\alpha$  (shown in dots) that represents the optimal image distortion needed to return the droplet image cross sections to a perfect circle. The true droplets, measured after collection in a quiescent state, are indeed nearly perfect spheres.

In order to measure the time-resolved geometry of the produced droplets, images with minimal spatial variation in the scan distortion are desirable. Therefore, microscope images were recorded far downstream from the capillary collection inlet. However, this raises an additional problem, since the droplets began to become disorganized in their orientation downstream. An algorithm was developed in MATLAB to automatically identify the inner and outer radii of droplets even when they appear to overlap.

The recorded images were first transformed by an affine transformation,  $A$ , to reverse the image distortion factor,

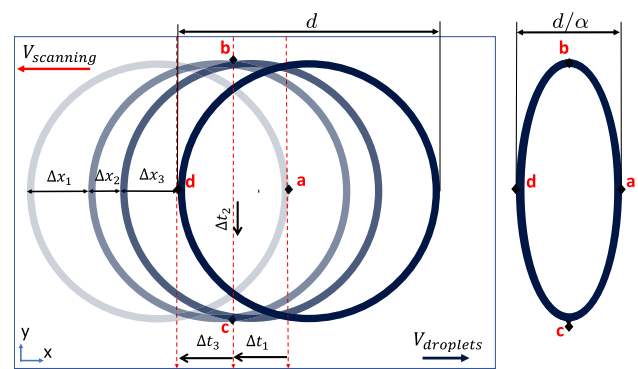


**Fig. 2** The confocal microscope scans line by line in the -x direction, while the droplets motion is in the +x direction. The droplet is illustrated as a blue circle moving on the left side in the physical scanning field and on the right side as it would appear in the distorted image field. Initially, scanner observes the most downstream edge of the droplet (marked ‘a’). As the scanning proceeds for a duration  $\Delta t_1$ , the scanner observes point ‘b’, which has already moved forward a distance of  $\Delta x_1$  during that elapsed time. The scanner then rapidly reaches point ‘c’, after an additional  $\Delta t_2$ , which is the time it takes for the scanner to scan the line from ‘b’ to ‘c’, and in this time the droplet moves forward another  $\Delta x_2$ . Finally, the droplet moves forward another  $\Delta x_3$  in  $\Delta t_3$  before the most upstream point ‘d’ is scanned. The droplet image therefore appears squashed by a factor  $\alpha$  in the resulting image, distorted from its true diameter  $d$  to a perceived diameter  $d/\alpha$

$\alpha$ , converting the elliptical shape into a circle according to Brannan et al. (2012):

$$A = \begin{bmatrix} \alpha & 0 \\ 0 & 0 \end{bmatrix}. \tag{3}$$

The images were then contrast-enhanced to identify only those regions of high fluorescence intensity in the outer shell that are in the focal plane of the confocal microscope. The depth of field (section thickness) of the microscope was minimized by modifying the pinhole aperture to achieve a thickness of  $7.17 \mu\text{m}$ , which is typically a small fraction of the droplet outer dimension. In a given image, anywhere from 10% to 20% of the droplets were centered in the focus plane and thus amenable to measurement. The stretching and contrast enhancement are shown in Fig. 4a and b.

Once the droplet images were transformed, ‘Laplacian of Gaussian’ edge detection was used, with thresholding, to identify the edges of the inner and outer interfaces of each droplet. Then, Hough-transform-based circle finding (implemented in MATLAB as ‘imfindcircles’) was employed to detect these nearly circular edges, as shown in Fig. 4c. Note that this circle finding is highly dependent on the ability of the affine transformation to render the original ellipses into approximate circles; it fails to detect ellipses with high eccentricity.

The circles detected by the Hough transform did not optimally overlap the thresholded droplet edges, as shown



**Fig. 3** (Top) Microscope image of the collector capillary tube, showing its increasing inner radius and the changing appearance of the scanned droplets. (Middle) Enlargements of individual droplets at three streamwise locations, illustrating the difference in image distortion. (Bottom) The distortion factor  $\alpha$  as a function of downstream distance  $x$ , calculated (dots) to optimally return the droplet image to a perfect circle and predicted (red line) from the flow velocity using equation 2

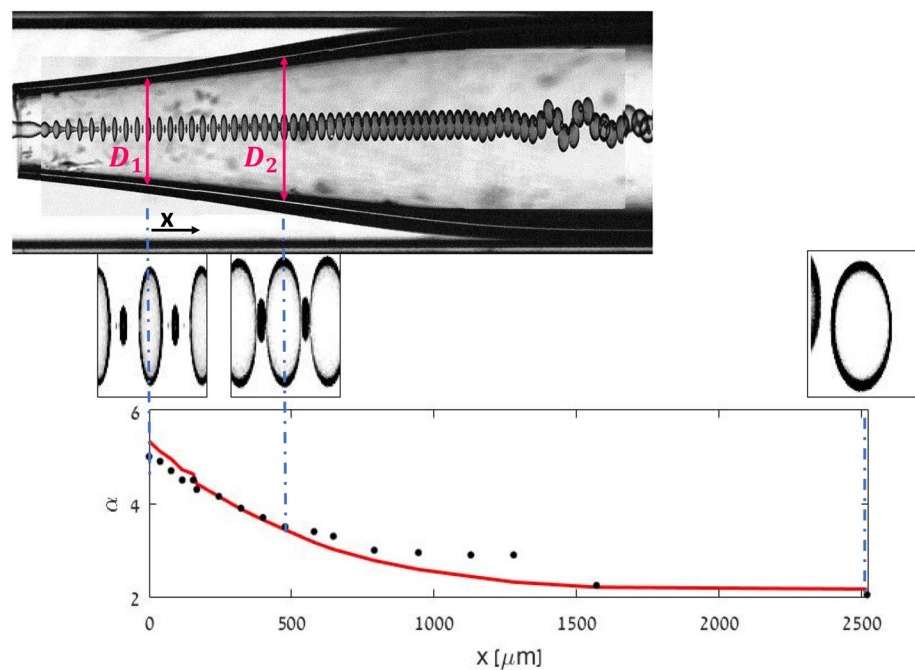
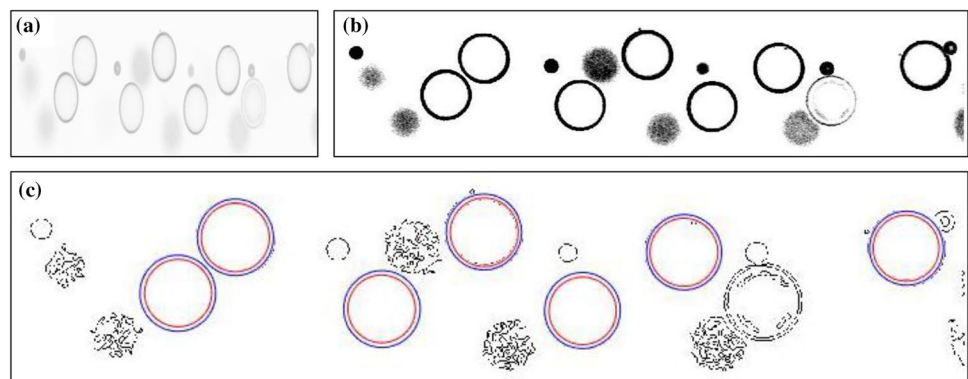


**Fig. 4** **a** The original 8-bit intensity map of the microscope fluorescence channel. **b** The intensity map after affine transformation and with contrast enhancement, in which the bottom 95% and top 1% of pixel intensity values are saturated. **c** The thresholded edges with inner and outer circles detected by the Hough transform technique



in Fig. 5a, where the black edges and red/blue circles are not aligned. An additional optimization step was employed in which the circle centers and radii were found which maximize the overlap between the detected circle perimeter and the droplet edge (within some constrained search domain). These optimal circles were then scored based on the extent of the overlap and circles with poor fit were excluded, finally obtaining the image shown in Fig. 5b.

The droplet detection algorithm was then used to measure the geometrical parameters of droplets recorded over 500–1000 images per experiment, in order to measure time evolution of the droplet geometry. The polydispersity,  $\gamma$ , for droplets with radius,  $r$ , averaged over all the images, was also calculated according to Pal et al. (2011):

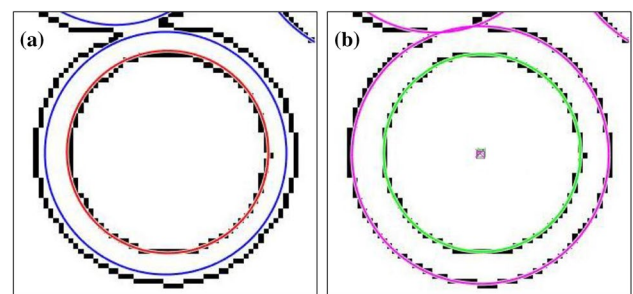


**Fig. 5** **a** The edges of the droplet interfaces, shown in black, against the circles found using the Hough transformation, shown in red and blue. **b** The corrected locations of the inner and outer circles, using a constrained optimization technique that maximizes the overlap between the circle and the edges

$$\gamma = \frac{\langle r^2 \rangle}{\langle r \rangle^2} \tag{4}$$

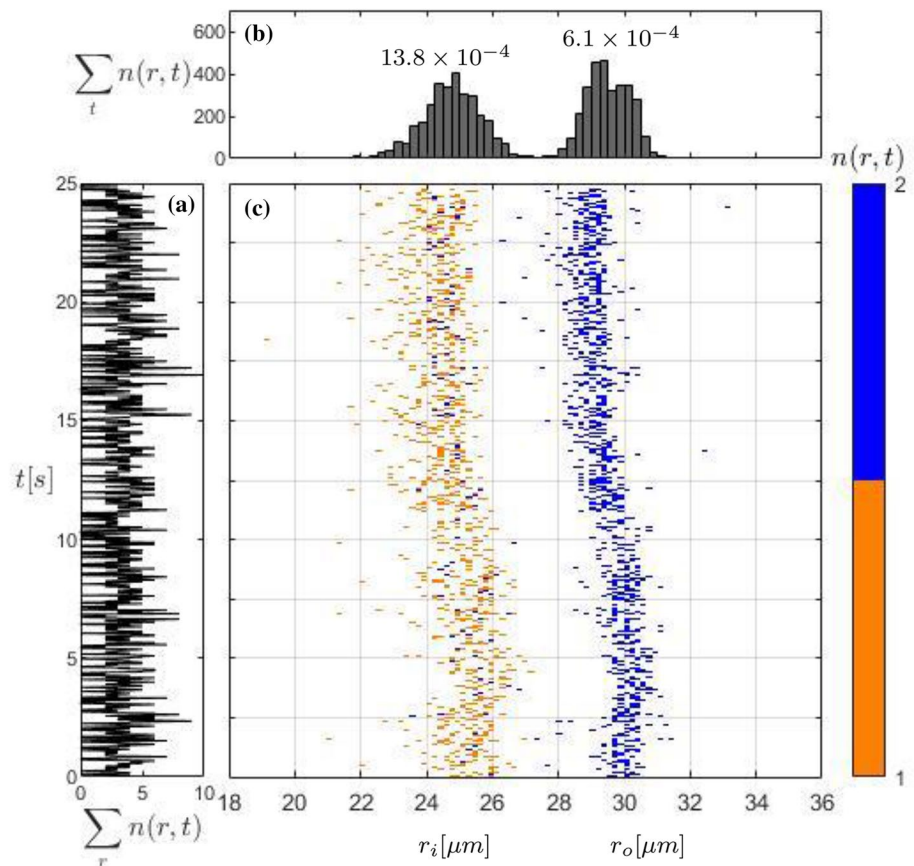
for both the inner and outer droplet radii. The time evolution of the inner and outer radii of droplets produced using the syringe-pump-driven device is shown in Fig. 6c and for the pressure-driven system in Fig. 7c. Both systems can produce nearly equivalent average polydispersity over time, as displayed above the histograms in Fig. 6b, although the syringe pump system is significantly more expensive and is known to suffer from periodic oscillations (Zeng et al. 2015). In both systems, the polydispersity of the inner droplet radius was about twice as high as that of the outer droplet radius, thereby affecting the polydispersity in the density, although not the ultimate radius of the produced particles. Moreover, the time-resolved geometry shows that the local polydispersity varied over a timescale of more than 5s. Even with this variation, the typical, average polydispersity of the outer radius was between  $4\text{--}6 \times 10^{-4}$ , which is significantly better than the  $3 \times 10^{-3}$  reported for commercial polystyrene tracer particles (Cospheric Orange Polyethylene Microspheres, UVPMS-BO-1.00). For even stricter polydispersity requirements, either better flow conditioning is needed, or the production should be limited to short duration, well-monitored runs.

Figure 4 also shows the presence of small, satellite droplets in the vicinity of the primary double-emulsion droplets. These satellite droplets were not included in the polydispersity analysis because they are made entirely of the oil phase and thus are significantly lighter than the double-emulsion droplets and were easily separated by gravity after the double-emulsion droplets are solidified and collected. The number of satellite droplets generated can also be reduced by the adjustment of the surfactant concentration and nozzle geometry (Nabavi et al. 2015).

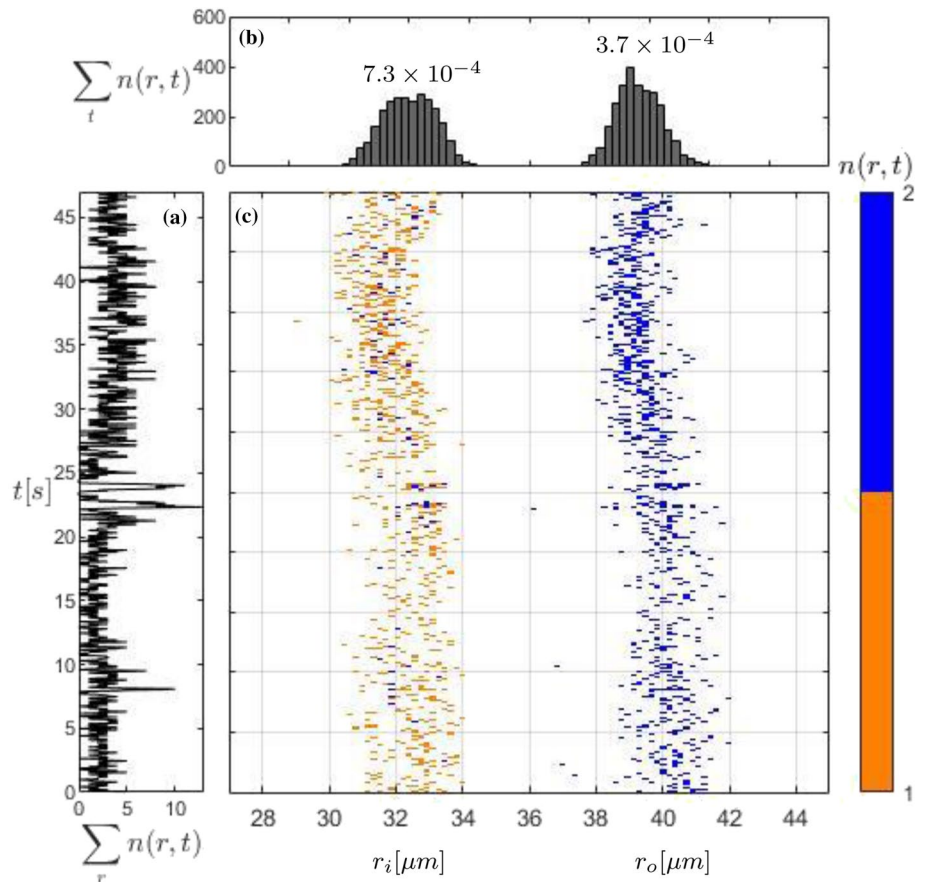
Once the droplets were produced, they were irradiated with UV light to cross-link the polymer in the outer shell, generating a solid particle (with a liquid core). The measured radii were then used to calculate the range of densities obtainable, according to equation 1, which depends primarily on the density of the inner salt solution,  $\rho_i$ , and on the relative thickness of the outer hard shell,  $\Delta r/r_i$ , as illustrated in Fig. 8. The typical shell thickness ranged from 6–22% of the inner radius for droplets with outer radii between 28 and 73  $\mu\text{m}$  and could be controlled by modifying the flowrates of the three phases. By varying the salt concentration, an entire spectrum of different density particles can be generated, with identical or varying sizes and fluorescence properties.

In addition to the in situ characterization of the droplets in the flow, upstream of the UV-solidification process, the

**Fig. 6** Time-resolved droplet geometry for syringe-pump-driven droplet production over 1000 frames recorded at 40 fps. **a** The number of detectable, in-focus, droplets per frame. **b** The cumulative histogram of all detectable droplets, separated to inner and outer droplet radii (denoted with subscripts  $i$  and  $o$ , respectively). The polydispersity,  $\gamma$ , for each dimension is denoted above the maximum in the histogram. **c** The time variation of the detected droplet histogram for the duration of a single experiment, where  $n(r, t)$  is the number of droplets detected at time  $t$  with radius in the bin containing  $r$



**Fig. 7** Time-resolved droplet geometry for pressure-driven droplet production over 1000 frames recorded at 21.5 fps. Labels are the same as those described in Fig. 6



particles were also collected downstream, after solidification, and imaged by bright-field, fluorescent, and scanning electron microscopy (Helios Nanolab G3 FEI with Elstar Column), as illustrated in Fig. 9a,c,e. Also, to demonstrate the hardened outer shell of the particles, a sample of solidified particles was mechanically crushed between two glass slides and then imaged using all three techniques, as shown in Fig. 9b,d,f, where the hollow core and fractured or deformed outer shell is clearly visible.

### 4 Optical discrimination of density

An important use for custom density particles is multi-phase flow measurements, in which a field of inertial particle motion is measured independently of the passive tracer particles used to track the continuous-phase flow field. The fluorescent dye used in the outer shell allows the particles to be discriminated from non-fluorescent particles using simple optical filters. In typical PIV measurements, non-fluorescent particles reflect the light of an incident laser sheet into a camera. Fluorescent particles absorb the incident laser light and then emit light at a higher wavelength, which can be collected in another camera, after filtering out the reflected light. The key to this process is obtaining a sufficiently large

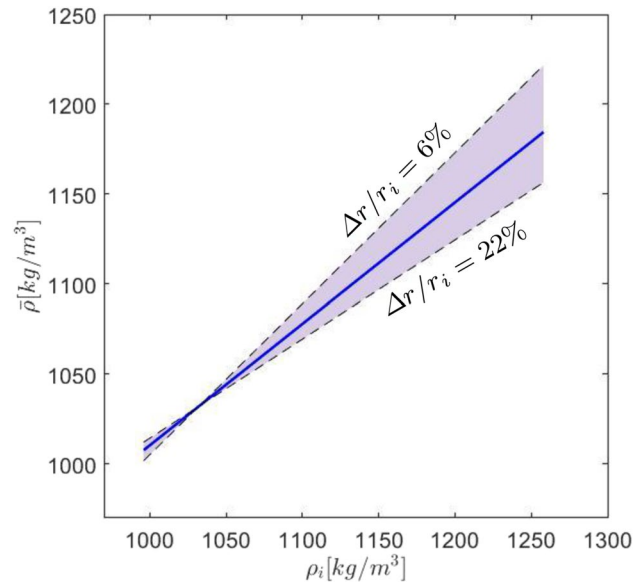


**Fig. 8** The average density of the final double-emulsion droplets as a function of the density of the inner phase salt solution, shown in the solid blue line. The dashed-black lines indicate the effect of the relative thickness of the outer shell,  $\Delta r/r_i$ , on the average density



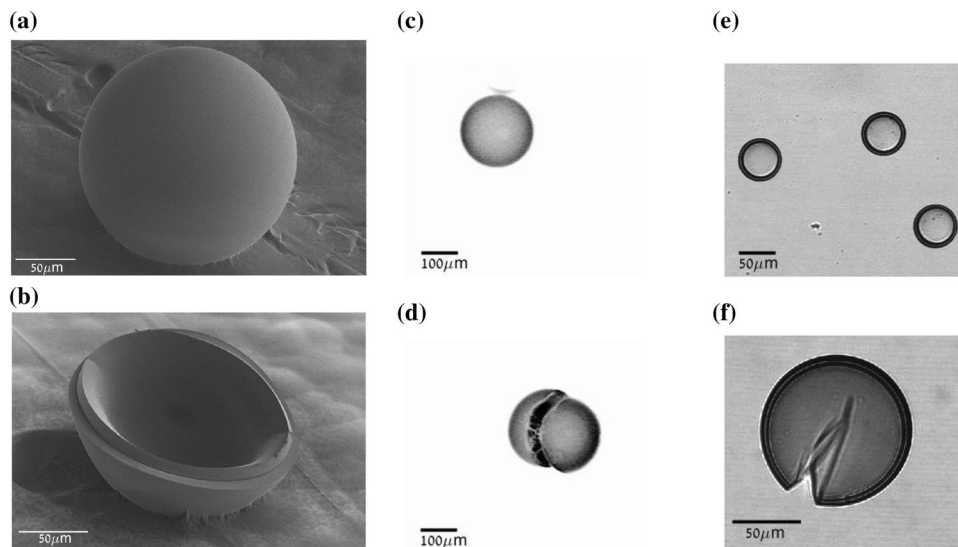


**Fig. 9** In the top row, solid cured particles, imaged by **a** scanning electron microscopy (SEM), **c** fluorescent microscopy, and **e** bright field microscopy. In the bottom row, a mechanically-crushed, cured particle is imaged by all three techniques, **b** SEM, **d** fluorescent microscopy, and **f** bright field microscopy, illustrating the solid outer shell. The SEM image was scanned with a tilt angle of 52°. The

bright field images were made using a 25× water immersion objective for the crushed particles, within a droplet of water, and a 10× dry objective for the whole particles. The fluorescent images employed a 5× dry objective. The particles shown here were drawn from a different batch than those analyzed in Figs. 6 and 7, hence the size difference

fluorescence response from the particles to be detected. We first compare the fluorescence response of the custom particles to commercial particles by using the confocal microscope as a spectrophotometer and then demonstrate their practical use in a simple, macroscale settling experiment.

As described above, Nile Red was selected as the fluorescent dye for the outer shell because it absorbs visible light in a range typical of many laboratory PIV systems, like the Nd:YLF system used here (Litron LD-30 527), which operates at 527 nm. The emission spectrum of Nile Red depends on its solvent (and co-solvent), and both acetone and DMSO were used as cosolvents. The custom particles were compared to commercial polystyrene tracer particles (Cospheric Orange Polyethylene Microspheres, UVPMS-BO-1.00) designed to absorb the same range of wavelengths.

The fluorescent emission spectrum of un-dyed and dyed custom particles and commercial particles was measured under an incident (confocal scanning) laser at 514 nm, with 3-nm-wide bins in emission wavelength,  $\lambda_e$ . The light emission from the individual particles was then averaged over ten measurements, to produce the emission spectra shown in Fig. 10a, and normalized with respect to the commercial particles in Fig. 10b. The fluorescence response for the custom particles was nearly twice as strong as that of the commercial particles. Also, note that the commercial particles have comparable reflection and emission magnitudes, whereas the custom particles have lower reflection compared to emission. This lower reflection may be desirable in many applications, but, if

necessary, the reflection performance of the custom particles could be improved by different additives to the outer shell, in place of the fluorescent dye, including nanoscale metallic or glass powders.

Having established the competitive fluorescence performance of the custom particles, a simple settling demonstration was conducted at the macroscale, to validate the particles for practical laboratory use. Two sets of custom particles were generated with roughly the same diameter, 150–170  $\mu\text{m}$ , but significantly different densities, 1.15 g/mL and 1.01 g/mL. The denser particles were produced using a 20% CsCl water solution and then dyed with Nile Red in DMSO; the lighter particles were produced from plain DI water with surfactant and left un-dyed. Both particles were mixed in a small glass tank and then allowed to settle freely, under gravity. The concentration of heavier particles was about 1/4 of that of the lighter particles. Two cameras (Phantom Veo 340L and Veo 440L) were focused and calibrated on the same region of a 1 mm thick laser sheet passing through the center of the tank to record the settling particles. One camera was equipped with a notch filter (Chroma ZET532nf) to block out the reflected laser light; the other with a band-pass filter (Chroma ZET532/10x) to block out all but the reflected laser light. The setup is shown in Fig. 11.

The images recorded from the two cameras were numerically corrected for the distortion due to the different camera angles using commercial PIV software (LaVision Davis 10.1). The reflection image in Fig. 12a showed both particles, whereas the fluorescent image in Fig. 12c showed only the

**Fig. 10** **a** Light intensity,  $I$ , of emission (for fluorescent particles) and reflection (for un-dyed particles), as a function of emission wavelength,  $\lambda_e$ . The commercial particles are shown as a black-dashed line; the custom density particles are shown in red (acetone cosolvent) and blue (DMSO cosolvent). The green line represents the reflection intensity of un-dyed custom particles. **b** The light intensities of the custom particles,  $I$ , normalized by the intensity of the commercial particles,  $I_c$ . The incident laser is at 514 nm

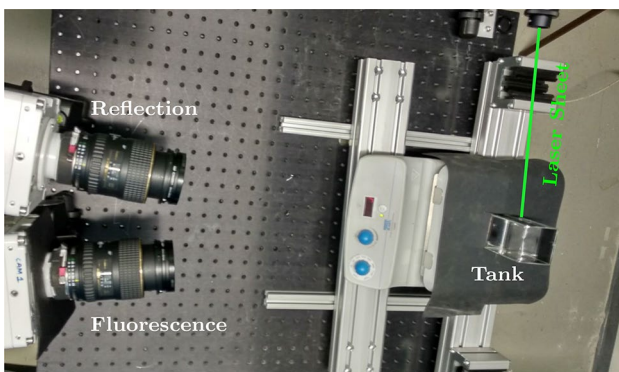
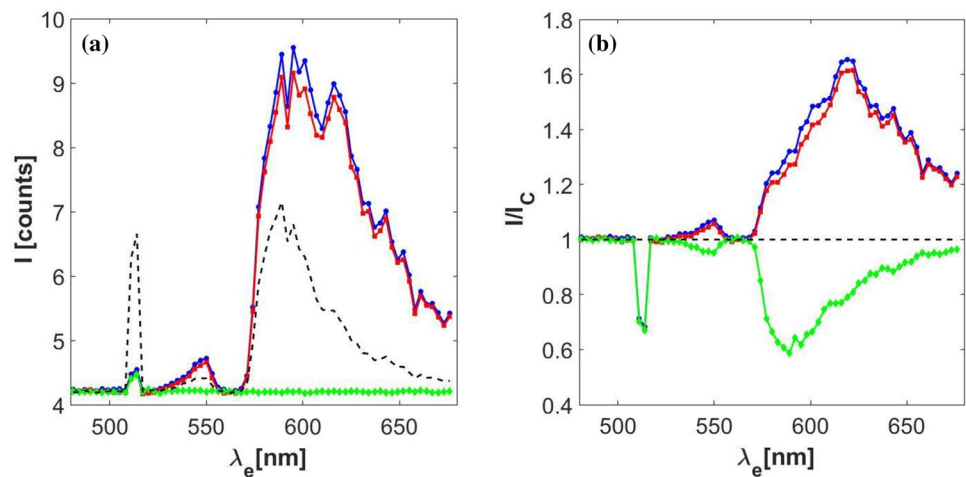


**Fig. 11** A settling experiment using two cameras focused on a laser sheet passing through a small glass tank over a stirring plate. Each camera was equipped with a separate filter to discriminate between the reflected light of the lighter particles and the fluorescent emission of the heavier particles

heavier, fluorescent particle. The fluorescent image was then used as a mask to mark the fluorescent particles appearing in the reflection image. This same mask could then be used to subtract the fluorescent particles from the reflection image entirely. Note that the fluorescent particles nearly saturate the image, whereas the reflection signal is substantially weaker. The concentration of dye can be easily adjusted to produce the desired balance between the two signals. Immediately after stirring, the heavy particles were evenly distributed in the tank. After 150 s of settling, most of the heavier fluorescent particles left the interrogation window, as shown in Fig. 12b,d. In this simple demonstration, the custom particles allowed for simple optical discrimination of density, despite their identical sizes.

## 5 Conclusions

A technique for producing inexpensive, custom density tracer particles was developed using a novel application of double-emulsion droplets. The inner phase of the droplet was used to

fine-tune the overall density by modifying the concentration of a salt solution. The outer phase of the droplet was used to create custom fluorescent properties and to solidify the resulting particle into a solid form, by lithography. Using widely available cesium chloride, a range of particle densities between 0.997 and 1.222 g/mL was achieved, for a wide range of particle diameters between 60 and 400  $\mu\text{m}$ . The droplets were produced by a co-flow glass capillary device that could be operated by syringe pumps or common laboratory air pressure. The low polydispersity of the droplets, with respect to both size and density, was verified by an optical particle-measurement algorithm. The particles were shown to produce a better fluorescence response than expensive, commercial particles and lower polydispersity. Finally, the particles were tested in a simple settling demonstration to show how the optical density discrimination technique can be easily performed using these custom particles without significant image processing. The present application of microfluidic, double-emulsion techniques for producing tracer particles allows for significant improvements in polydispersity- and density control over existing tracer manufacturing technologies that are based on grinding solid materials or rapidly dispersing droplets by mixing.

## Flow parameters for Droplet production

Stable droplet production depends on independently adjusting the flowrates of the three phases (Utada et al. 2005). Table 2 provides general guidelines for the production of particles with outer diameters in the range of 60–100  $\mu\text{m}$ . The specific flowrates ultimately depend on the exact shape of the pulled capillary tip and the cleanliness of the capillaries and must be adjusted iteratively for each production run to achieve a stable stream of droplets.

Once a stable droplet production is achieved, small disturbances in the flows can disrupt the production, particularly with the syringe pump approach, where periodic oscillations

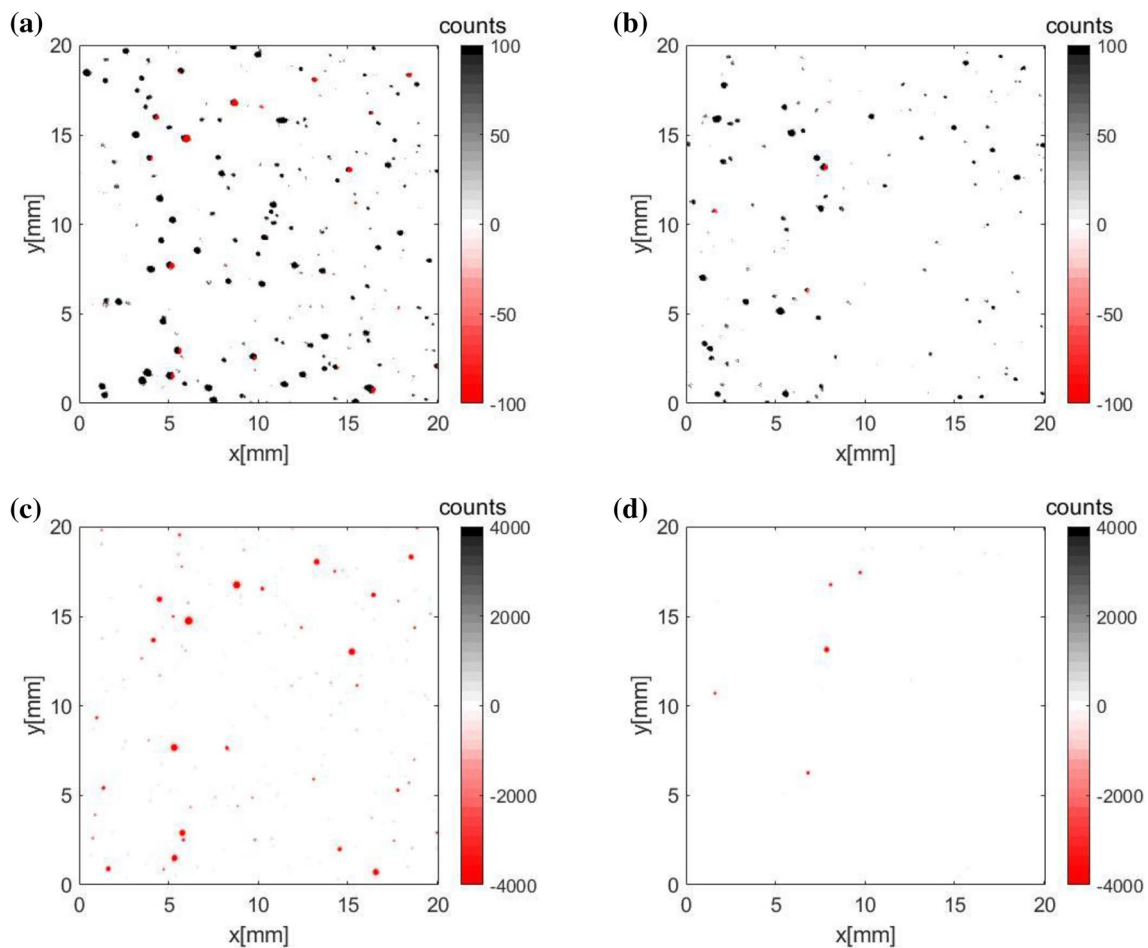


**Fig. 12** The reflection images including both the dyed and un-dyed particles, immediately after stirring (a) and after 150 s of settling (b). The heavier particles are marked in red, based on a mask produced from the fluorescent images; the lighter particles are marked in black.

The fluorescent images containing only the emission from the heavier particles, at the same two time instants in (c) and (d). The significant reduction by settling of the number of heavy particles in (d) compared to (c) is apparent

**Table 2** General ranges of flowrates and pressure settings used to produce the droplets

System	Inner phase	Middle phase	Outer phase
Syringe Pumps [ $\mu\text{L}/\text{min}$ ]	2–8	2–8	200–220
Air pressure [psi]	1.5–3.5	1.5–3.5	9–12

due to the screw drive can perturb the flow. Therefore, the production must be monitored by microscope occasionally to detect any disruption. If a disruption in the droplet stream occurs, the flowrate of both inner and middle phases must be increased to reestablish a thick, stable (double) jet, after which they are then reduced gradually until stable production resumes.

**Acknowledgements** This research was supported by Grant No. 2014208 from the United States-Israel Binational Science Foundation

(BSF) and Grant No. 1704/17 from the Israel Science Foundation. The authors thank Eyal Barn for his help with the particle analysis algorithm, the Russell Berrie Nanotechnology Institute for assistance with the electron microscope imaging, and the anonymous referees for useful comments.

## References

- Adrian RJ, Westerweel J (2010) Particle image velocimetry. Cambridge University Press, Cambridge
- Dabiri D, Pecora C (2019) Particle tracking velocimetry. IOP Publishing, London
- Mei R (1996) Velocity fidelity of flow tracer particles. *Exp Fluids* 22(1):1–13
- Melling A (1997) Tracer particles and seeding for particle image velocimetry. *Meas Sci Technol* 8(12):1406–1416
- Eaton JK, Fessler JR (1994) Preferential concentration of particles by turbulence. *Int J Multiph Flow* 20(94):169–209
- Crowe CT, Gore RA, Troutt TR (1985) Particle dispersion by coherent structures in free shear flows. *Part Sci Technol* 3:149–158

- Hetsroni G (1989) Particles-turbulence interaction. *Int J Multiphase Flow* 15(5):735–746
- Zhao LH, Andersson HI, Gillissen JJJ (2010) Turbulence modulation and drag reduction by spherical particles. *Phys Fluids* 22(8):5111–5111
- Lee J, Lee C (2015) Modification of particle-laden near-wall turbulence: effect of stokes number. *Phys Fluids* 27(2):21
- Guha A (2008) Transport and deposition of particles in turbulent and laminar flow. *Annu Rev Fluid Mech* 40(1):311–341
- Lindken R, Merzkirch W (2002) A novel PIV technique for measurements in multiphase flows and its application to two-phase bubbly flows. *Exp Fluids* 33(6):814–825
- Cheng Y, Pothos S, Diez FJ (2010) Phase discrimination method for simultaneous two-phase separation in time-resolved stereo PIV measurements. *Exp Fluids* 49(6):1375–1391
- Khalitov DA, Longmire EK (2002) Simultaneous two-phase PIV by two-parameter phase discrimination. *Exp Fluids* 32(2):252–268
- Elhimer M, Praud O, Marchal M, Cazin S, Bazile R (2017) Simultaneous PIV/PTV velocimetry technique in a turbulent particle-laden flow. *J Vis* 20(2):289–304
- Hoque MM, Mitra S, Sathe MJ, Joshi JB, Evans GM (2016) Experimental investigation on modulation of homogeneous and isotropic turbulence in the presence of single particle using time-resolved PIV. *Chem Eng Sci* 153:308–329
- Kondo C, Miyamoto J (2017) Production of inexpensive inorganic fluorescent tracer for particle image velocimetry of in-cylinder flows in engines. In: *The 28th international symposium on transport phenomena*
- Pedocchi F, Martin JE, García MH (2008) Inexpensive fluorescent particles for large-scale experiments using particle image velocimetry. *Exp Fluids* 45(1):183
- Tauro F, Porfiri M, Grimaldi S (2013) Fluorescent eco-particles for surface flow physics analysis. *AIP Adv* 3(3):396
- Nisisako T, Torii T, Higuchi T (2004) Novel microreactors for functional polymer beads. *Chem Eng J* 101(1–3):23–29
- Dendukuri D, Pregibon DC, Collins J, Hatton TA, Doyle PS (2006) Continuous-flow lithography for high-throughput microparticle synthesis. *Nat Mater* 5(5):365–369
- Nan L, Cao Y, Yuan S, Shum HC (2020) Oil-mediated high-throughput generation and sorting of water-in-water droplets. *Microsyst Nanoeng* 6(1):37
- Utada AS, Lorenceau E, Link DR, Kaplan PD, Stone HA, Weitz DA (2005) Monodisperse double emulsions generated from a microcapillary device. *Science* 308:537–541
- Bong KW, Chapin SC, Pregibon DC, Baah D, Floyd-Smith TM, Doyle PS (2011) Compressed-air flow control system. *Lab Chip* 11(4):743–747
- Zhao CX, Chen D, Hui Y, Weitz DA, Middelberg APJ (2017) Controlled generation of ultrathin-shell double emulsions and studies on their stability. *ChemPhysChem* 18(10):1393–1399
- Chong DT, Liu XS, Ma HJ, Huang GY, Han YL, Cui XY, Yan JJ, Xu F (2015) Advances in fabricating double-emulsion droplets and their biomedical applications. *Microfluid Nanofluid* 19(5):1071–1090
- Utada AS, Chu LY, Fernandez-Nieves A, Link DR, Holtze C, Weitz DA (2007) Dripping, jetting, drops, and wetting: the magic of microfluidics. *MRS Bull* 32(9):702–708
- Brannan DA, Esplen MF, Gray JJ (2012) *Geometry*. Cambridge University Press, Cambridge
- Pal N, Verma SD, Singh MK, Sen S (2011) Fluorescence correlation spectroscopy: an efficient tool for measuring size, size-distribution and polydispersity of microemulsion droplets in solution. *Anal Chem* 83(20):7736–7744
- Zeng W, Jacobi I, Beck DJ, Li S, Stone HA (2015) Characterization of syringe-pump-driven induced pressure fluctuations in elastic microchannels. *Lab Chip* 15(4):1110–1115
- Nabavi SA, Vladislavljević GT, Gu S, Ekanem EE (2015) Double emulsion production in glass capillary microfluidic device: Parametric investigation of droplet generation behaviour. *Chem Eng Sci* 130:183–196

**Publisher's Note** Springer Nature remains neutral with regard to jurisdictional claims in published maps and institutional affiliations.